Hydrostatic Hamiltonian particle mesh (HPM) methods for atmospheric modeling.

Seoleun Shin*   Sebastian Reich*   Jason Frank**

March 17, 2011

Abstract

We develop a hydrostatic Hamiltonian particle mesh (HPM) method for efficient long-term numerical integration of the atmosphere. In the HPM method, the hydrostatic approximation is interpreted as a holonomic constraint for the vertical position of particles. This can be viewed as defining a set of vertically buoyant horizontal meshes, with the altitude of each mesh point determined to satisfy the hydrostatic balance condition, and with particles modeling horizontal advection between the moving meshes. We implement the method in a vertical slice model and evaluate its performance for the simulation of idealized linear orographic flow in both dry and moist environments. The HPM method is able to capture the basic features of the gravity wave to a degree of accuracy comparable to that reported in the literature. Numerical solution in the moist experiment indicates the influence of moisture on wave characteristics is represented reasonably well and the reduction of momentum flux is in good agreement with theoretical analysis.

1   Introduction

In recent years efforts have been made to extend the use of Hamiltonian particle-mesh (HPM) methods for atmospheric modeling (e.g. Frank et al. (2002); Frank & Reich (2004); Cotter et al. (2004); Shin & Reich (2009)). An important issue in atmospheric modeling, particularly for climate simulation, is the numerical conservation of mass of air, water, and long-lived tracers (Thuburn 2008). The hydrostatic HPM method has some advantages with respect to this issue in that it conserves mass locally and satisfies an exact advection equation for long-term simulations. The key idea is to approximate horizontal motion along the lines of the Hamiltonian particle-mesh method while the vertical motion is discretized as a moving mesh method. Lin (2004) has also discussed the reduction of dimensionality of physical problems through floating vertical coordinates in the context of a finite volume dynamical core. In this article we present the hydrostatic HPM method and test the scheme for idealized orographic flows. We demonstrate that HPM is able to properly represent fundamental processes such as

*Universität Potsdam, Institut für Mathematik, Am Neuen Palais 10, D-14469 Potsdam, Germany
**CWI, P.O. Box 94079, 1090 GB Amsterdam, the Netherlands

the generation of gravity waves due to orographic forcing and the influence of moist processes on the character of the orographic wave. Compared to previous numerical studies Durran & Klemp (1983) (Hereafter DK83) and Pinty et al. (1995) (Hereafter P95) for hydrostatic orographic flows, the wave generation is well-represented in our model.

In the following sections we explain details of the HPM method and how we represent moving meshes to enforce time-dependent hydrostatic balance. Then we discuss the results of numerical experiments and propose further work with the HPM method.

2   The Hydrostatic HPM

The hydrostatic Hamiltonian particle-mesh (HPM) method is derived for a vertical slice model, using Eulerian coordinates $(x, z) \in \Omega \subset \mathbb{R}^2$ and Lagrangian labels $(a, b) \in \Omega$. We denote discrete approximations of dependent variables over the Eulerian grid with Latin indices, and those over a discrete label space with Greek indices. For example, $f_{\alpha,\gamma}$ is an approximation to $f(a, c)$ at a grid point $(a_\alpha, c_\gamma) = (\alpha \Delta a, \gamma \Delta c)$ in label space, where Δa, Δc are mesh sizes and $\alpha, \gamma \in \mathbb{Z}$. For mixed Eulerian-Lagrangian approximations, we use a form such as $f_{i,\gamma} \approx f(x_i, c_\gamma)$. More details about those mixed approximation will be given in the following paragraphs.

The hydrostatic HPM method is different in nature from the nonhydrostatic HPM (Shin & Reich 2009) in that the vertical motion is discretized using a moving mesh. We define time-dependent Lagrangian particles with x-positions denoted by $x_{\alpha,\gamma+1/2}(t)$, and vertically buoyant mesh points with z-coordinates $z_{i,\gamma}(t)$. As indicated by the indexing, the horizontal position of the mesh point is fixed in the Eulerian frame, while its vertical position is fixed in the Lagrangian frame, i.e. $z = z(x, c)$. We define horizontal basis functions with support centered at the mean of two vertically moving mesh points, that is, at $(x_i, z_{i,\gamma+1/2})$ with $z_{i,\gamma+1/2} = (z_{i,\gamma+1} + z_{i,\gamma})/2$. The basis functions, denoted by $\psi_{i,\gamma+1/2}(x)$, are non-negative and satisfy the partition of unity property

$$\sum_i \psi_{i,\gamma+1/2}(x) = 1 \tag{2.1}$$

for all $(x, z) \in \Omega$. We also introduce the scaled basis functions

$$\hat{\psi}_{i,\gamma+1/2}(x) = \frac{\psi_{i,\gamma+1/2}(x)}{\Delta x}. \tag{2.2}$$

It is natural to use the same basis function at x_i independent of the value of γ. Hence we will use the simpler notation $\psi_i(x)$ and $\hat{\psi}_i(x)$. A basis function having the desired properties is the cubic B-spline with support radius $2\Delta x$.

A Lagrangian particle with x-position $x_{\alpha,\gamma+1/2}$ carries a mass $m_{\alpha,\gamma+1/2}$ and a potential temperature $\theta_{\alpha,\gamma+1/2}$. Note that we do not request that $\theta_{\alpha,\gamma+1/2} = \theta_{\gamma+1/2}$, i.e., lines of constant $c_{\gamma+1/2}$ need not be lines of constant potential temperature. Additionally, in the case of moist simulations, a particle also carries a moisture budget, which is commonly represented by the total mixing ratio $r_{t_{\alpha,\gamma+1/2}}$. The moisture can experience phase changes and in this study we consider only those between cloud water and water vapor. The three quantities $(m_{\alpha,\gamma+1/2}, \theta_{\alpha,\gamma+1/2}, r_{t_{\alpha,\gamma+1/2}})$ remain constant under unsaturated conditions, but $\theta_{\alpha,\gamma+1/2}$ may

vary when latent heat is released in association with phase changes of water. The quantity of $m_{\alpha,\gamma+1/2}$ and $r_{t_{\alpha,\gamma+1/2}}$ remains always constant. Regardless of the saturated/unsaturated condition, the moist static energy is conserved so that the scheme can be energetically consistent.

Here we consider simple problems of air flows in a hydrostatic balance, which are a good approximation for orographic flow arising due to moderate surface terrains.

2.1 Density approximation

The density $\rho_{i,\gamma+1/2}(t) \approx \rho(x_i, z_{i,\gamma+1/2})$ is approximated by

$$\rho_{i,\gamma+1/2}(t) = \frac{1}{z_{i,\gamma+1}(t) - z_{i,\gamma}(t)} \left[\sum_{\alpha} m_{\alpha,\gamma+1/2} \hat{\psi}_i(x_{\alpha,\gamma+1/2}(t)) \right]. \tag{2.3}$$

Conservation of mass is encoded in the identity

$$\sum_{i,\gamma} \rho_{i,\gamma+1/2}(t) \Delta x [z_{i,\gamma+1}(t) - z_{i,\gamma}(t)] = \sum_{i,\gamma} \left[\sum_{\alpha} m_{\alpha,\gamma+1/2} \hat{\psi}_i(x_{\alpha,\gamma+1/2}(t)) \right] \Delta x$$

$$= \sum_{\alpha,\gamma} m_{\alpha,\gamma+1/2} \left[\sum_{i} \psi_i(x_{\alpha,\gamma+1/2}(t)) \right] \tag{2.4}$$

$$= \sum_{\alpha,\gamma} m_{\alpha,\gamma+1/2},$$

due to (2.1). The product of density and potential temperature, i.e., $\mu = \theta\rho$, is a primitive variable, approximated at (vertically moving) mesh points $(x_i, z_{i,\gamma+1/2})$. The approximation for $\mu_{i,\gamma+1/2}$ is

$$\mu_{i,\gamma+1/2}(t) = \frac{1}{z_{i,\gamma+1}(t) - z_{i,\gamma}(t)} \left[\sum_{\alpha} \theta_{\alpha,\gamma+1/2} m_{\alpha,\gamma+1/2} \hat{\psi}_i(x_{\alpha,\gamma+1/2}(t)) \right], \tag{2.5}$$

and we obtain conservation via

$$\sum_{i,\gamma} \mu_{i,\gamma+1/2}(t) \Delta x [z_{i,\gamma+1}(t) - z_{i,\gamma}(t)] = \sum_{\alpha,\gamma} \theta_{\alpha,\gamma+1/2} m_{\alpha,\gamma+1/2}. \tag{2.6}$$

Other thermodynamic quantities are now easily approximated over $(x_i, z_{i,\gamma+1/2})$ using the standard identities

$$T = \theta\pi, \qquad \pi = \left(\frac{\mu}{\mu_0} \right)^{\kappa/(1-\kappa)}, \tag{2.7}$$

where $\mu_0 = p_0/R$ is a constant reference value, $c_p = c_v/(1-\kappa)$, and $\kappa = R_d/c_p = 2/7$, where R_d is the ideal gas constant for dry air.

2.2 Equations of motion and discrete hydrostatic balance

Since we work with the hydrostatic approximation, the vertical motion does not contribute to the kinetic energy and we obtain the discrete approximation

$$\mathcal{T} = \frac{1}{2} \sum_{\alpha,\gamma} m_{\alpha,\gamma+1/2} |\dot{x}_{\alpha,\gamma+1/2}|^2. \tag{2.8}$$

The potential energy is approximated from the analytic expression:

$$\mathcal{V}_{\text{analytic}} = \int_{\Omega} \left[c_v \mu_0 \left(\frac{\mu}{\mu_0} \right)^{1/(1-\kappa)} + g\rho z \right] dxdz. \tag{2.9}$$

For our given approximations this becomes

$$\mathcal{V} = \sum_{i,\gamma} \left[c_v \mu_0 \left(\frac{\mu_{i,\gamma+1/2}}{\mu_0} \right)^{1/(1-\kappa)} + g\rho_{i,\gamma+1/2} z_{i,\gamma+1/2} \right] \Delta x \Delta z_{i,\gamma+1/2}, \tag{2.10}$$

where for ease of notation we introduce the following abbreviation:

$$\Delta z_{i,\gamma+1/2} = z_{i,\gamma+1} - z_{i,\gamma}. \tag{2.11}$$

The equations of motion are now obtained from the Lagrangian functional

$$L = \int \mathcal{L} dt, \tag{2.12}$$

where $\mathcal{L} = \mathcal{T}$ - $\mathcal{V}$. The associated Euler-Lagrange equations are straightforward to derive. Since $\dot{z}_{i,\gamma}$ does not feature in $\mathcal{L}$, we obtain a holonomic constraint for each $z_{i,\gamma}$ instead. The nonlinear constraint equations are coupled in the index γ but not in i. Hence we have to essentially solve a decoupled set of discretized, one-dimensional, nonlinear elliptic equations in the vertical. Note that this also holds true in three dimensions. The appropriate boundary conditions are $z_{i,0} = 0$ and $z_{i,M} = H$ for the bottom and top surfaces. It is easy to include orography into this approach by simply setting $z_{i,0} = z_s(x_i)$, where $z_s(x_i)$ is the height of the surface at x_i. The discrete variational principle leads to

$$m_{\alpha,\gamma+1/2} \ddot{x}_{\alpha,\gamma+1/2} = F^G_{x,\alpha,\gamma+1/2} + F^P_{x,\alpha,\gamma+1/2}, \tag{2.13}$$

where the gravitational force applied on the particle is

$$F^G_{x,\alpha,\gamma+1/2} = -g \, m_{\alpha,\gamma+1/2} \sum_i [z_{i,\gamma+1/2} \nabla_x \psi_i(x_{\alpha,\gamma+1/2})], \tag{2.14}$$

and the pressure gradient force is

$$F^P_{x,\alpha,\gamma+1/2} = -c_p m_{\alpha,\gamma+1/2} \theta_{\alpha,\gamma+1/2} \sum_i \left[\left(\frac{\mu_{i,\gamma+1/2}}{\mu_0} \right)^{\kappa/(1-\kappa)} \nabla_x \psi_i(x_{\alpha,\gamma+1/2}) \right]. \tag{2.15}$$

Störmer-Verlet time-stepping leads to the explicit update

$$m_{\alpha,\gamma+1/2} \left[x_{\alpha,\gamma+1/2}^{n+1} - 2x_{\alpha,\gamma+1/2}^n + x_{\alpha,\gamma+1/2}^{n+1} \right] = \Delta t^2 \left[F_{x,\alpha,\gamma+1/2}^{G,n} + F_{x,\alpha,\gamma+1/2}^{P,n} \right]. \tag{2.16}$$

For a simpler notation in the following, we define $\overline{\mu}_{i,\gamma+1/2} = \mu_{i,\gamma+1/2}\Delta z_{i,\gamma+1/2}$ and $\overline{\rho}_{i,\gamma+1/2} = \rho_{i,\gamma+1/2}\Delta z_{i,\gamma+1/2}$. To complete the time-step at t_{n+1}, we obtain the new vertical positions $z_{i,\gamma}^{n+1}$ that satisfy the discrete hydrostatic balance condition

$$0 = F_{z,i,\gamma}^G + F_{z,i,\gamma}^P, \tag{2.17}$$

with

$$F_{z,i,\gamma}^G = -\frac{g}{2} \left[\overline{\rho}_{i,\gamma+1/2} + \overline{\rho}_{i,\gamma-1/2} \right], \tag{2.18}$$

and

$$\begin{aligned} F_{z,i,\gamma}^P &= c_v \mu_0 \left[\left(\frac{\mu_{i,\gamma+1/2}}{\mu_0} \right)^{1/(1-\kappa)} - \left(\frac{\mu_{i,\gamma-1/2}}{\mu_0} \right)^{1/(1-\kappa)} \right] \\ &\quad - c_p \left[\mu_{i,\gamma+1/2} \left(\frac{\mu_{i,\gamma+1/2}}{\mu_0} \right)^{\kappa/(1-\kappa)} - \mu_{i,\gamma-1/2} \left(\frac{\mu_{i,\gamma-1/2}}{\mu_0} \right)^{\kappa/(1-\kappa)} \right] \\ &= -\kappa c_p \mu_0 \left[\left(\frac{\mu_{i,\gamma+1/2}}{\mu_0} \right)^{1/(1-\kappa)} - \left(\frac{\mu_{i,\gamma-1/2}}{\mu_0} \right)^{1/(1-\kappa)} \right], \end{aligned} \tag{2.19}$$

by again applying the discrete variational principle. These equations are solved subject to the boundary conditions $z_{i,0} = z_s(x_i)$ and $z_{i,M} = H$. Note that with particles horizontally fixed, $F_{z,i,\gamma}^G$ is constant. We use the relation

$$F_{z,i,\gamma}^P = -\kappa c_p \mu_0 \left[\left(\frac{\overline{\mu}_{i,\gamma+1/2}}{\mu_0} \right)^{1/(1-\kappa)} \Delta z_{i,\gamma+1/2}^{1/(\kappa-1)} - \left(\frac{\overline{\mu}_{i,\gamma-1/2}}{\mu_0} \right)^{1/(1-\kappa)} \Delta z_{i,\gamma-1/2}^{1/(\kappa-1)} \right] \tag{2.20}$$

and

$$\frac{\partial}{\partial z_{i,\gamma}} \Delta z_{i,\gamma+1/2}^{1/(\kappa-1)} = \frac{\partial}{\partial z_{i,\gamma}} (z_{i,\gamma+1} - z_{i,\gamma})^{1/(\kappa-1)} = \frac{1}{1-\kappa} \Delta z_{i,\gamma+1/2}^{1/(\kappa-1)} \Delta z_{i,\gamma+1/2}^{-1}, \tag{2.21}$$

plus related formulas to set up a Newton iteration for finding $z_{i,\gamma+1/2}$. The diagnostic estimation of the vertical velocity of the moving grid can be approximated by

$$w_{i,\gamma+1/2}^{n+1/2} = \frac{1}{\Delta t} (z_{i,\gamma+1/2}^{n+1} - z_{i,\gamma+1/2}^n). \tag{2.22}$$

We illustrate the moving meshes in response to the generation of orographic wave associated with an isolated hill in the vertical slice model (Fig. 1). If there is a disturbance that generates imbalance on the vertically stratified layers, meshes move vertically to find a new position $z_{i,\gamma+1/2}^{n+1}$ that satisfies hydrostatic balance. The particles lay half-way between the adjacent horizontal meshes so that they also adjust vertically conforming to the buoyant
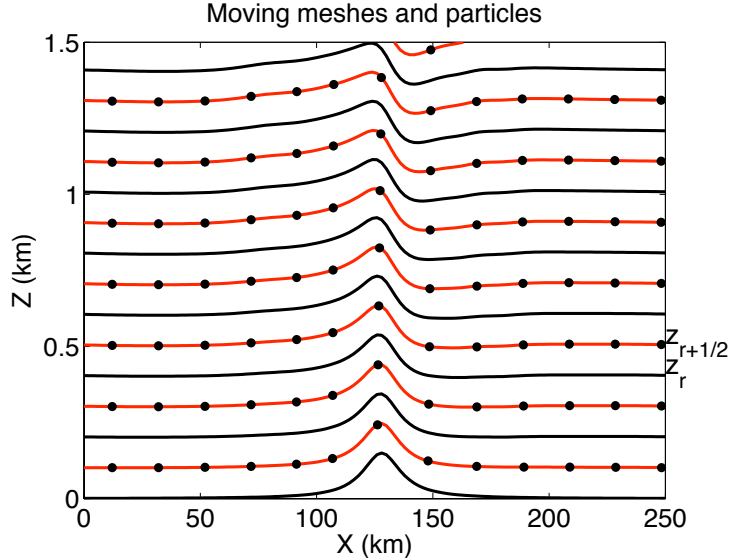
Figure 1: Schematic descriptions of particles conforming to a moving mesh due to an isolated hill. Vertical grids (z_γ) are denoted by black lines and the mean of two vertically moving meshes, $z_{i,\gamma+1/2} = (z_{i,\gamma+1} + z_{i,\gamma})/2$ by red lines. We plot every 20th particle (Black dots) in each layer.

meshes. A similar moving mesh approach was combined with an Eulerian finite volume scheme and semi-Lagrangian advection in (Lin 2004).

We did not use numerical diffusion for tests in this study, but spurious small scale perturbations are filtered using a Helmholtz operator on the thermodynamic quantities over the grid (Frank et al. 2002). The Helmholtz operator is applied directly in the Lagrangian such that Hamiltonian structure is maintained. In the current context, we smooth $\overline{\rho}$, $\overline{\mu}$, z and the Exner function π. Frank et al. (2005) showed that the combination of this regularization and Störmer-Verlet time-stepping modifies the dispersion relation in a manner equivalent to a two-time-level semi-implicit time discretization for the linearized shallow-water equations. Let $H_i^{i'}$ denote a discrete approximation to the Helmholtz operator

$$H = 1 - \alpha_x^2 \frac{\partial^2}{\partial x^2} \tag{2.23}$$

over the x grid subject only to x and its periodic boundary conditions. Here $\alpha_x \geq 0$ is a given smoothing length. Then a smoothed $\widetilde{\mu}_i$ is defined as the solution of

$$\sum_{i'} H_i^{i'} \widetilde{\mu}_{i'} = \overline{\mu}_i. \tag{2.24}$$

Likewise we obtain $\widetilde{\pi}$ using the Helmholtz operator. Note that now $\widetilde{\mu}/\Delta z_{i,\gamma+1/2}$ and $\widetilde{\rho}/\Delta z_{i,\gamma+1/2}$ replace μ and ρ in (2.10).

6

3   Numerical experiments with orography

We evaluate the performance of our scheme by testing the generation of gravity waves due to an idealized orography. Details of the experiments are listed briefly in Table 1. The aim of these tests is to examine if the hydrostatic HPM method is capable of capturing general features of gravity waves in the presence of orography. For this purpose we use the tests in the linear hydrostatic flow regime reported in DK83 and P95. As is pointed out in a number of references in the literature, an appropriate upper boundary layer is essential in numerical simulations of orographic flow to prevent the reflection of waves back into the domain. The portion of the domain where a dissipative boundary condition is put into operation is often called a "sponge layer". In our experiments we apply such a boundary condition only to the zonal wind. The sponge layer in DK83 is defined by

$$u^+ = u^- + \frac{\Delta t}{2} \tau(z)(u^- - U), \tag{3.1}$$

where u^- is an updated zonal velocity using (2.13), U a constant zonal wind speed given at the initial time, Δt is a time interval, and u^+ a new velocity. In DK83 $\tau(z)$ is defined by

$$\tau(z) = \begin{cases} 0, & \text{for } z \leq z_B \\ -\frac{\chi}{2}\left(1 - \cos\frac{z-z_B}{z_T-z_B}\pi\right), & \text{for } 0 \leq \frac{z-z_B}{z_T-z_B} \leq 0.5 \\ -\frac{\chi}{2}\left[1 + \left(\frac{z-z_B}{z_T-z_B} - \frac{1}{2}\right)\pi\right], & \text{for } 0.5 \leq \frac{z-z_B}{z_T-z_B} \leq 1 \end{cases} \tag{3.2}$$

where χ is a constant, z_T is the top of the domain, and z_B is the bottom of the sponge layer. We choose the constant $\chi = 20 \ h^{-1}$, with which an optimal solution is produced in the experiments of this study. We have observed excessive dissipation or instability with much larger or smaller than this value, respectively. Meanwhile the type of sponge layer in P95 is given such that

$$u^+ = (1 - \beta)u^- + \beta U. \tag{3.3}$$

The coefficient $\beta = \beta_v$ for the vertical sponge layer in P95 is defined by

$$\beta_v = \begin{cases} 0, & \text{for } z < z_B \\ \left(\frac{z-z_B}{z_T-z_B}\right)^2, & \text{for } z_B < z < z_T, \end{cases} \tag{3.4}$$

and similarly the coefficient $\beta = \beta_h$ for lateral sponge zones is given by

$$\beta_h = \begin{cases} \cos^2\left[\frac{\pi}{2}\left(\frac{x}{x_D}\right)\right], & \text{for } 0 < x < x_D \\ \cos^2\left[\frac{\pi}{2}\left(\frac{x_L-x_D}{x_D}\right)\right], & \text{for } x_L - x_D < x < x_L \\ 0, & \text{otherwise,} \end{cases} \tag{3.5}$$

where x_L is the lateral size of the domain and x_D is the thickness of the sponge zone. We choose the P95 type of lateral sponge zone since we obtain an optimal solution close to the

analytic solution with this boundary condition. The Coriolis parameter is set to be zero for all tests. We use a bell-shaped profile for the orography represented by

$$h(x) = h_0 \left(\frac{a^2}{x + a^2} \right). \tag{3.6}$$

Initially we begin with the peak height $h_0 = 0$ and increase h_0 gradually during the early stage of the integration until h_0 becomes 1 m high. The isolated hill is placed at the center of the domain. The number of particles is 2 per cell and the total number of particles per layer is kept uniform.

Test	Details	Description
T1	$U = 20$ m/s, $a = 10$ km, $N = 0.0196$ s^{-1}	Linear hydrostatic flow in DK83
T2	$U = 32$ m/s, $a = 16$ km, $N = 0.0187$ s^{-1}	Linear hydrostatic flow in P95
T3	$U = 20$ m/s, $a = 10$ km, $N = 0.0132$ s^{-1}	Linear dry/moist flow in DK83

T1: Linear hydrostatic flow
Figure 2 shows the zonal wind perturbation ($u' = u - U$) and vertical velocity perturbation ($w' = w$). The vertical wind is approximated by the velocity of vertically moving meshes defined in (2.22). The size of spatial domain is $L_x = 180$ km and $L_z = 16$ km, and the atmosphere is isothermal with the temperature $T_0 = 250$ K as in DK83. The bottom of the sponge layer z_B is 8 km. For the lateral sponge zone, we choose the thickness $x_L = 2$ km. The smoothing length $\alpha_x = 1$ km. The spatial resolution in DK83 was 2 km, but we choose it to be 1 km since we obtain more accurate solution with the doubled spatial resolution. The vertical velocity perturbation is better captured in our hydrostatic model with the increase in the spatial resolution. We can integrate the equation with the time-step size of 18 s. Figure 2 also shows time tendency of the energy, and the profile of the vertical flux of horizontal momentum M, which is defined by

$$M = \int_{-\infty}^{\infty} \rho u' w' dx, \tag{3.7}$$

in terms of Reynolds stress and this is normalized by pressure drag on the surface approximated by

$$D = \frac{-\pi}{4} \rho_0 N U h_0^2, \tag{3.8}$$

for the linear mountain wave (Durran & Klemp 1983). As shown in (3.8), the buoyancy frequency N controls the magnitude of the surface drag given mountain height and mean wind speed. The simulation is stable as implied by the energy tendency and the wave structure and the magnitude of the perturbation are in good agreement with the reference solution presented in DK83. For example, the local minimum of the zonal wind perturbation around $z = 5$ km is correctly captured as seen by the contour line of -24 $\times$ 10^{-3} m/s (see

Fig. 1a in DK83 for the analytic solution). The normalized momentum flux during the quasi-steady state is about 0.97 (Fig. 2) and this is quite close to the theoretical value 1. We observe that the coefficient χ for the vertical sponge layer influences the magnitude of the perturbation and the behavior of the vertical momentum flux (not shown). The larger χ becomes, the weaker becomes the momentum flux.
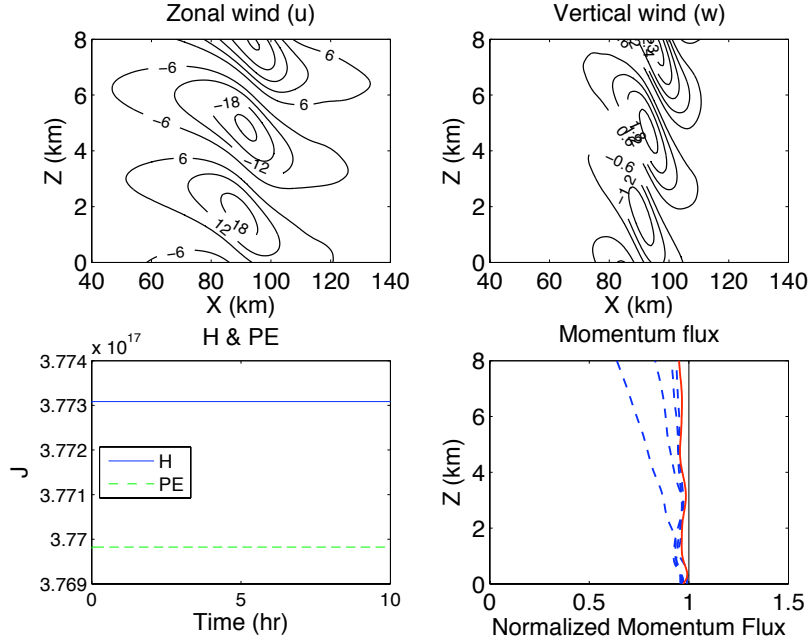

Figure 2: The zonal wind (u'), vertical velocity (w'), time tendency of the total energy (H) and potential energy (PE), and vertical profile of the normalized momentum flux. We display here $1000u'$ and $1000w'$. The contour interval is 6×10^{-3} m/s for the zonal wind and 0.6×10^{-3} m/s for the vertical wind. They are the solution at $t = 10$ h, when it is quasi-steady. The momentum flux at 10 h is colored red and the flux at earlier integration times displayed in blue dash lines. See more details in text.

T2: Linear hydrostatic flow in P95

The height of the hill h_0 is the same as DK83, but the hill is broader and the uniform initial wind speed is stronger (32 m/s instead of 20 m/s). Also the domain size is larger with $L_x = 512$ km and $L_z = 20$ km. We use the same spatial resolution $\Delta x = 3.2$ km and $\Delta z = 0.25$ km as in P95. In our simulations Δt can be up to 35 s with the smoothing scale $\alpha_x = 3.2$ km for the result shown in this article. In P95, z_B is not explicitly given, but they suggest that $z_B = L_z - \lambda_z$, where λ_z is the vertical wave length of the dominant wave. The wave length is $\lambda_z = 2\pi U/N$ so that the bottom of the sponge layer z_B is estimated to be 9.29 km. For the lateral sponge zone, we choose the thickness $x_L = 2$ km as in T1. Figure 3a shows the result from the experiment with the P95 type of vertical sponge layer and Figure 3b shows the result with the DK83 type of the sponge layer. In both simulations we use the P95 type of lateral sponge zones. The wave structure is similar to each other and to the reference solution in P95, but the magnitude of the perturbation in Figure 3a is slightly weaker. The momentum flux resolved is well represented in both experiments and close to the analytical
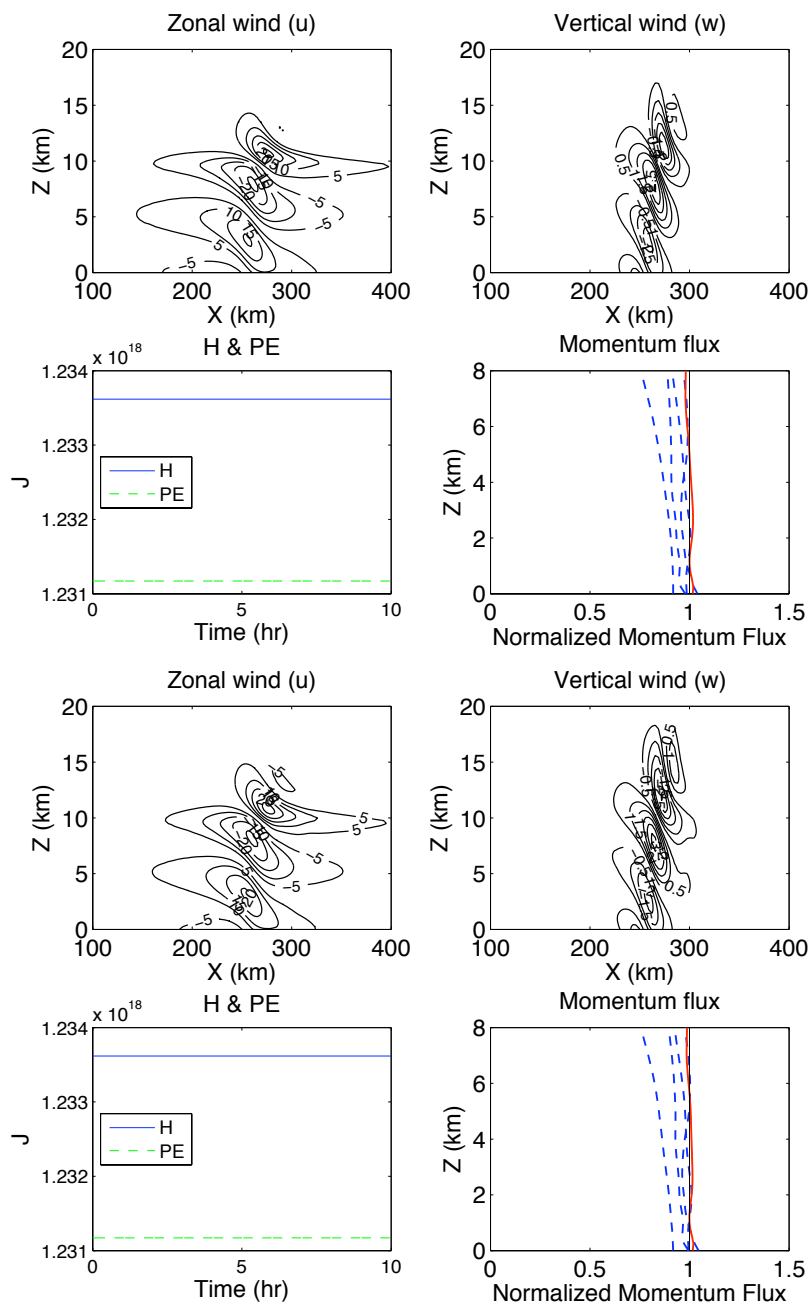
9

estimation.

Figure 3: The same as Figure 2, except the contour interval is 5×10^{-3} m/s for the zonal wind and 0.5×10^{-3} m/s for the vertical wind. (a) T2 with the vertical sponge layer of P95. (b) T2 with the vertical sponge layer of DK83. The P95 type of lateral sponge zones are used in both simulations.

4   Representation of moist process

We consider here highly simplified condensation and evaporation processes explicitly resolved over particles. We summarize the notation for the variables associated with moist processes:

$$
\begin{aligned}
&m_d &&\text{dry air mass component} \\
&m_v &&\text{mass of water vapor component} \\
&m_c &&\text{mass of liquid water component} \\
&r_v &&\text{mixing ratio of water vapor, } r_v = m_v/m_d \\
&r_c &&\text{cloud water, } r_c = m_c/m_d \\
&r_s &&\text{mixing ratio of liquid water} \\
&r_t &&\text{total moisture content of an air parcel, } r_t = r_v + r_c \\
&L &&\text{the latent heat of vaporization at } 0°\text{C} = 2.5 \times 10^6 \text{ J/kg} \\
&R_v &&\text{the specific gas constant of water vapor} = 461.5 \text{ J/(kg·K)}
\end{aligned}
$$

To account for liquid water loading and water vapor in the reversible moist process, the ideal gas equation in the moist environment can be expressed by

$$
p = \rho R_d T \frac{1 + r_v/\epsilon}{1 + r_t}, \tag{4.1}
$$

where $\epsilon = R_d/R_v \approx 0.622$, the ratio of gas constant of dry air to water vapor. Accordingly, hydrostatic balance is defined by

$$
\frac{d\pi}{dz} = -\frac{g}{c_p \theta} \frac{1 + r_t}{1 + r_v/\epsilon}. \tag{4.2}
$$

The relation between π and $\mu = \rho\theta$ becomes

$$
\pi = \left[\frac{\mu}{\mu_0} \left(\frac{1 + \frac{r_v}{\epsilon}}{1 + r_t} \right) \right]^{\frac{\kappa}{(1-\kappa)}}. \tag{4.3}
$$

Given an initial condition, the density over the position of a particle $\mathbf{x}_{\alpha,\gamma+1/2}$ can be approximated by

$$
\rho_{\alpha,\gamma+1/2} = \frac{p_{\alpha,\gamma+1/2}}{R T_{\alpha,\gamma+1/2}} \frac{1 + r_{v_{\alpha,\gamma+1/2}}/\epsilon}{1 + r_{t_{\alpha,\gamma+1/2}}}. \tag{4.4}
$$

We assign the (total) mass of the "moist particle", $m_{\alpha,\gamma+1/2,t_0} \approx \rho_{\alpha,\gamma+1/2,t_0} \Delta a \Delta c$. This is done at the initial time and the mass of the particle remains unchanged in time. Using the hydrostatic equation (4.2), we calculate the vertical mesh position $z_{i,\gamma+1/2}$ and the pressure gradient force for the particles is given by

$$
F^P_{x,\alpha,\gamma+1/2} = -c_p m_{\alpha,\gamma+1/2} \, \theta_{\alpha,\gamma+1/2} \sum_i \left[\left(\frac{\mu_{i,\gamma+1/2}}{\mu_0} \frac{1 + r_{v_{i,\gamma+1/2}}/\epsilon}{1 + r_{t_{i,\gamma+1/2}}} \right)^{\kappa/(1-\kappa)} \nabla_x \psi_i(x_{\alpha,\gamma+1/2}) \right]. \tag{4.5}
$$

Even in the absence of phase changes, $r_{s_{\alpha,\gamma+1/2,t}}$ on the particles at time t needs to be calculated if the pressure and temperature approximated at the position have been changed. We use Bolton's formula (1980) for the saturated vapor pressure

$$e_{s_{\alpha,\gamma+1/2,t}}(T) = 6.11 \exp\left[\frac{17.67(T_{\alpha,\gamma+1/2,t} - 273)}{243.5 + T_{\alpha,\gamma+1/2,t} - 273}\right], \tag{4.6}$$

e_s is in hPa. Then we obtain the saturation mixing ratio r_s

$$r_{s_{\alpha,\gamma+1/2,t}} \approx \epsilon \frac{e_{s_{\alpha,\gamma+1/2,t}}}{(p_{\alpha,\gamma+1/2,t} - e_{s_{\alpha,\gamma+1/2,t}})}. \tag{4.7}$$

The thermodynamic equations for the phase conversion processes are similar to those for the moisture budget in Klemp and Wilhelmson (1978), but we do not include any numerical diffusion terms or sub-grid turbulent parameterization. The prognostic equations for the two moist components, water vapor and condensed liquid water, and potential temperature are given by

$$\frac{dr_v}{dt} = \delta(r_v, r_c)\frac{dr_s}{dt},$$
$$\frac{dr_c}{dt} = -\delta(r_v, r_c)\frac{dr_s}{dt}, \tag{4.8}$$
$$\frac{d\ln\theta}{dt} = -\frac{L}{c_p T}\frac{dr_v}{dt}.$$

The Heaviside function $\delta(r_v, r_c)$ has been introduced to represent phase conversions that occur under the conditions:

$$\delta(r_v, r_c) = \begin{cases} 1, & \text{for } r_v \geq r_s \text{ or } r_c > 0 \\ 0, & \text{for } r_v < r_s \text{ and } r_c = 0. \end{cases}$$

We assume that the phase conversions take places over each particle and the moist components compose the total mass of the particle. The latent heat of vaporization (L) is indeed varying with the temperature, but we take it as constant for the numerical experiments, where the effect is negligible for the purpose of this study. The total water content r_t is conserved in the absence of rain and turbulent mixing.

Once the parcel is saturated, $r_v - r_s > 0$, the excess is converted into liquid water and added to r_c. The new r_v becomes equal to r_s. The change of saturation mixing ratio Δr_s and the associated change of the temperature ΔT through the phase conversion is approximated by

$$\Delta r_s \approx \frac{r_s - r_v}{1 + L^2 r_s/(c_p R_v T^2)}, \tag{4.9}$$

$$\Delta T \approx -\frac{L\Delta r_s}{c_p}. \tag{4.10}$$

The derivation of the equation for Δr_s are described in Appendix A. To ensure the value of r_c and r_v remain positive and r_t is invariant, we limit $\Delta r_s = \max(\Delta r_s, r_v)$ for condensation

and $\Delta r_s = \min(\Delta r_s, -r_c)$ for evaporation. Subsequently, we can update the mixing ratio of water vapor, liquid water, and potential temperature using (4.8). Then, the height of mesh, $z_{i,\gamma+1/2,t}$ is calculated to satisfy a new hydrostatic balance after the occurrence of phase changes. To be consistent with (4.2) and (4.8) the energy ($\mathcal{E} = \mathcal{V} + \mathcal{T} + \mathcal{Q}$) of the system has contributions:

$$\mathcal{V} = \sum_{i,\gamma} \left[c_v \mu_0 \left[\frac{\mu_{i,\gamma+1/2}}{\mu_0} \left(\frac{1 + r_{v_{i,\gamma+1/2}}/\epsilon}{1 + r_{t_{i,\gamma+1/2}}} \right) \right]^{\frac{1}{(1-\kappa)}} + g\rho_{i,\gamma+1/2} z_{i,\gamma+1/2} \right] \Delta x \, \Delta z_{i,\gamma+1/2}, \quad (4.11)$$

$$\mathcal{T} = \frac{1}{2} \sum_{\alpha,\gamma} m_{\alpha,\gamma+1/2} |\dot{x}_{\alpha,\gamma+1/2}|^2, \tag{4.12}$$

$$\mathcal{Q} = L \sum_{\alpha,\gamma} r_{v_{\alpha,\gamma+1/2}} m_{\alpha,\gamma+1/2}. \tag{4.13}$$

$$\tag{4.14}$$

T3: Linear dry/moist hydrostatic flow in DK83

As described in the literature (e.g. DK83), the strength of the orographic wave can diminish when moisture is present. For the test T3 we use the same numerical set-up as for the test T1. The temperature profile is calculated given stability $N = 0.0132$ with the surface temperature $T_0 = 273$ K. The approximate Scorer parameter ($N^2/U^2 - U_{zz}/U$) can be constant with height as discussed in DK83. Figure 4a shows the result from the moist simulation with relative humidity RH = 100 % with $r_c = 0$ initially. In comparison to the dry simulation with RH = 0 % (Fig. 4b) the wave length is longer and the perturbation is weaker. The theoretical vertical wavelength $\lambda_z = 2\pi U/N$ might increase as the the stability is reduced due to the presence of moist processes. We approximate the first vertical half-wavelength of numerical solutions by examining the height at which the contour of isentropic surface becomes a mirror image of the isolated hill (DK83). The first vertical half-wavelength is about 4.5 km in the test without moisture (RH = 0 %), while it is about 7.5 km in the moist simulation. As done in DK83 we compare the momentum flux in this test with an analytical estimation using the approximate moist stability N_m suggested in Durran & Klemp (1982). For comparisons, we denote the reference magnitude of momentum flux of dry case by D defined in (3.8). The approximate moist stability is $N_m = 0.008$ s^{-1} at the surface given T_0 = 273 K and RH = 100 %. The momentum flux can be reduced to $0.61D$ theoretically, if N_m replaces N in (3.8). The vertical mean ($0 \sim 8$ km) of the momentum flux in Fig. 4a is about $0.56D$, which is lower than the expected value $0.61D$. Note that the momentum flux is about $0.4D$ instead of the theoretical estimation $0.47D$ in the partially cloudy case, while the difference is smaller in the everywhere cloudy case in DK83. In our simulation it is cloudy in the layer below about 5 km. To examine the effect of the cloudiness we retain the stability $N = 0.0132$, but increase the surface temperature to 280 K so that more latent heat can be released. This initial set-up yields the approximate moist stability $N_m = 0.006$ s^{-1} and the depth of cloudy layer extends to 6.5 km. The analytic estimation of surface drag is reduced to $0.46D$ with the decreased stability. The vertical mean of the momentum flux is about $0.47D$ in our simulation (Fig. 4c), which shows that the vertical profile of momentum flux becomes closer to the theoretical analysis as cloudiness increases. Those results from

13

T3 experiments indicate that the effect of moist process on the characteristics of mountain wave is reasonably represented by the hydrostatic HPM.

5 Discussions and outlook

We have extended the HPM method to a hydrostatic vertical slice model and evaluate its performance using some idealized tests of both dry and moist atmosphere. It is shown that the model captures the fundamental features of the orographic gravity wave and the results are quantitatively in good agreement to reference solutions. In particular, moist processes are newly implemented in an HPM model and the moist effect on the gravity wave is reasonably well reproduced. We show the potential of the hydrostatic HPM for a dynamical core suitable for climate simulations where the conservation of mass of air, water, and long-lived tracers is essential and no artifactual generation of energy is desirable.

As the methods stands, particles adjust vertically conforming to the moving mesh. However, we may need to consider a redistribution of particles when diabatic processes lead to a convective instability. A simple solution might be vertically exchanging particles between layers depending on heating/cooling, to resemble convection. In the future we will test such vertical exchanges of particles, aiming to develop a convective parameterization method for the hydrostatic HPM to describe cumulus convection and the response of larger-scale circulations. One can anticipate in such situations that the horizontal velocity distribution of particles can tend to be non-uniform. To prevent this, we may need to include a diffusion mechanism.

References

Cotter, C., Frank, J. & Reich, S. 2004 , Hamiltonian particle-mesh method for two-layer shallow-water equations subject to the ligid-lid approximation., SIAM J. Appl. Dyn. Sys **3**, 69–83.

Durran, D. R. & Klemp, J. B. 1982 , On the effects of moisture on the Brunt-Väisälä frequency., J. Atmos. Sci. **39**, 2152–2158.

Durran, D. R. & Klemp, J. B. 1983 , A compressible model for the simulation of moist mountain waves, Mon. Weather. Rev **111**, 2341–2361.

Frank, J. & Reich, S. 2004 , The Hamiltonian particle-mesh method for the spherical shallow water equations, Atmospheric Science Letters **5**, 89–95.

Frank, J., Gottwald, G. & Reich, S. 2002 , The Hamiltonian particle-mesh method, in M. Griebel & M. Schweitzer, eds, 'Meshfree Methods for Partial Differential Equations', Vol. 26 of **Lecture Notes in Computational Science and Engineering**, Springer-Verlag, Berlin Heidelberg, pp. 131–142.

Frank, J., Reich, S., Staniforth, A., White, A. & Wood, N. 2005 , Analysis of a regularized, time-staggered discretization method and its link to the semi-implicit method., Atm. Sci. Lett. **6**, 97–104.

Haltiner, G. J. & Williams, R. T. 1980 , Numerical prediction and dynamic meteorology, John Wiley, New York.

Lin, S.-J. 2004 , A "vertically Lagrangian" finite-volume dynamical core for global models., Mon. Weather. Rev. **132**, 2293–2307.

Pinty, J.-P., Benoit, R. & E. Richard, R. L. 1995 , Simple tests of a semi-implicit semi-Lagrangian model on 2D mountain wave problems, Mon. Weather. Rev **123**, 3042–3058.

Shin, S. & Reich, S. 2009 , Hamiltonian particle-mesh simulation for a non-hydrostatic vertical slice model, Atmospheric. Science. Letters **10**, 233–240.

Thuburn, J. 2008 , Some conservation issues for the dynamical cores of NWP and climate models, Journal of Computational Physics. **227**, 3715–3730.

A   Appendix

We use a simplified description of moist process suggested in Haltiner & Williams (1980). The condensation/evaporation of water vapor should satisfy the following relation

$$r_v + \Delta r_v = r_s(T + \Delta T, p), \tag{A.1}$$

during the time interval Δt assuming pressure is unchanged. This assumption is relevant for the hydrostatic regime. The term on the right-hand side can be approximated using the Taylor expansion,

$$r_s(T + \Delta T, p) \approx r_s(T) + \left(\frac{\partial r_s}{\partial T} \right)_p \Delta T. \tag{A.2}$$

Since

$$r_s = \epsilon \left(\frac{e_s}{p} \right), \tag{A.3}$$

$$\frac{de_s}{dT} = \frac{Le_s}{R_v T^2}, \tag{A.4}$$

we rewrite the Clasius-Clapeyron equation in terms of r_s like

$$\frac{dr_s}{dT} = \frac{Lr_s}{R_v T^2}, \tag{A.5}$$

Since $\Delta T = -L \Delta r_v / c_p$ by the thermodynamic law, we combine (A.1) and (A.2) and use (A.5) to express

$$r_v + \Delta r_v \approx r_s + \left(\frac{Lr_s}{R_v T^2} \right) \left(\frac{-L \Delta r_v}{c_p} \right). \tag{A.6}$$

Thus,

$$\Delta r_v \approx r_s - r_v + \left(\frac{L r_s}{R_v T^2} \right) \left(\frac{-L \Delta r_v}{c_p} \right). \tag{A.7}$$

If we rearrange this for Δr_v

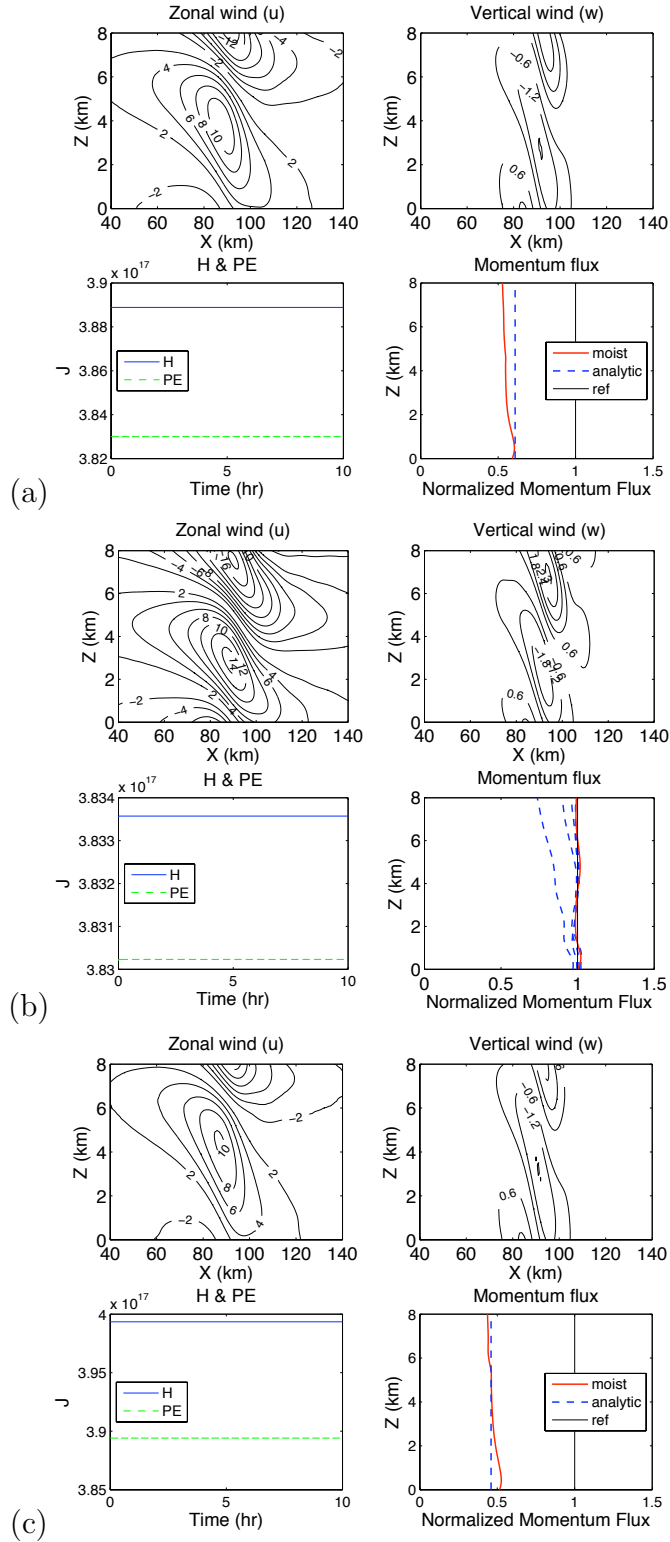$$\Delta r_v \approx \frac{r_s - r_v}{1 + \left(\frac{L^2 r_s}{c_p R_v T^2} \right)}. \tag{A.8}$$

Figure 4: The same as Figure 2, except some parameters given for the initial set-up. (a) Moist simulation with RH = 100 % and the surface temperature $T_0 = 273$ K. (b) The same as (a), but RH = 0. (c) RH = 100 % and $T_0 = 280$ K. See the details in text.